buildings

MDPI

Article

Mechanical Performance Prediction for Sustainable High-Strength Concrete Using Bio-Inspired Neural Network

Junbo Sun [1], Jiaqing Wang [2], Zhaoyue Zhu [3], Rui He [3], Cheng Peng [3], Chao Zhang [4], Jizhuo Huang [5,*], Yufei Wang [6,*] and Xiangyu Wang [6,*]

1 Institute for Smart City of Chongqing University, Chongqing University, Liyang 213300, China; tunneltc@gmail.com
2 College of Civil Engineering, Nanjing Forestry University, Nanjing 210037, China; jiaqingw@njfu.edu.cn
3 School of Architectural Engineering, Nanjing Institute of Technology, Nanjing 211167, China; zhuzhaoyue02002@163.com (Z.Z.); herui756@163.com (R.H.); pengcheng913@163.com (C.P.)
4 Hunan Provincial Key Laboratory of Geotechnical Engineering for Stability Control and Health Monitoring, Hunan University of Science and Technology, Xiangtan 411201, China; flyheartzc@hnust.edu.cn
5 College of Civil Engineering, Fuzhou University, 2 Xue Yuan Rd., University Town, Fuzhou 350116, China
6 School of Design and Built Environment, Curtin University, Perth 6102, Australia
* Correspondence: jzhuang@fzu.edu.cn (J.H.); wangyf0113_suz@163.com (Y.W.); Xiangyu.Wang@curtin.edu.au (X.W.)

Abstract: High-strength concrete (HSC) is a functional material possessing superior mechanical performance and considerable durability, which has been widely used in long-span bridges and high-rise buildings. Unconfined compressive strength (UCS) is one of the most crucial parameters for evaluating HSC performance. Previously, the mix design of HSC is based on the laboratory test results which is time and money consuming. Nowadays, the UCS can be predicted based on the existing database to guide the mix design with the development of machine learning (ML) such as back-propagation neural network (BPNN). However, the BPNN's hyperparameters (the number of hidden layers, the number of neurons in each layer), which is commonly adjusted by the traditional trial and error method, usually influence the prediction accuracy. Therefore, in this study, BPNN is utilised to predict the UCS of HSC with the hyperparameters tuned by a bio-inspired beetle antennae search (BAS) algorithm. The database is established based on the results of 324 HSC samples from previous literature. The established BAS-BPNN model possesses excellent prediction reliability and accuracy as shown in the high correlation coefficient (R = 0.9893) and low Root-mean-square error (RMSE = 1.5158 MPa). By introducing the BAS algorithm, the prediction process can be totally automatical since the optimal hyperparameters of BPNN are obtained automatically. The established BPNN model has the benefit of being applied in practice to support the HSC mix design. In addition, sensitivity analysis is conducted to investigate the significance of input variables. Cement content is proved to influence the UCS most significantly while superplasticizer content has the least significance. However, owing to the dataset limitation and limited performance of ML models which affect the UCS prediction accuracy, further data collection and model update must be implemented.

Keywords: high-strength concrete; unconfined compressive strength; beetle antennae search; back-propagation neural network; sensitivity analysis

check for updates

Citation: Sun, J.; Wang, J.; Zhu, Z.; He, R.; Peng, C.; Zhang, C.; Huang, J.; Wang, Y.; Wang, X. Mechanical Performance Prediction for Sustainable High-Strength Concrete Using Bio-Inspired Neural Network. *Buildings* **2022**, *12*, 65. https://doi.org/10.3390/buildings12010065

Academic Editor: Elena Ferretti

Received: 30 November 2021
Accepted: 5 January 2022
Published: 10 January 2022

1. Introduction

High-strength concrete (HSC) is a type of cementitious material that has uniaxial compressive strength (UCS) larger than 40 MPa [1–3]. The HSC composite exhibit outstanding mechanical strength, considerable durability, low permeability, and compact density. In addition, it satisfies special uniformity and performance requirements, which is superior to ordinary fabricated concrete [4–6]. HSC has been widely applied in long-span bridges because it sustains superior dead and live loading with fewer bridge piers and thus prolongs the service lifespan [7–9]. Meanwhile, HSC is also promising in high buildings because it enables oversized columns to yield more floor space and larger column spacing without detracting from lower floors [10–12]. The behaviour of connectors when embedded in the HSC, such as the shear resistance and ductility, has been investigated by several researchers [13,14]. The general behaviour of HSC beams was investigated based on the mid span deflection, failure mode, and crack growth [15]. HSC can also be served as the main construction material accompanied by several advanced technologies, such as building information modelling, 3D printing technology, etc. [16–23]. Besides, solid waste materials, such as waste glass and recycled aggregate, have the potential to be applied in HSC to overcome the strength shortcomings of the waste itself [24–31]. Therefore, HSC incorporated with solid wastes has the benefits of both strength enhancement and sustainable prospect [32–34].

For HSC composites, the uniaxial compressive strength (UCS) is the most significant factor in the design procedure before application. Numerous experiments of HSC by the research facilities have been carried out to investigate the relationship between UCS and its composite constituents. However, the progress is costly and lengthy because too many trial batches have to be prepared to explore desirable mechanical performance with a large number of influencing variables. The pre-configuration of equipment also consumes time and resources. Some conventional evaluation strategies have been used to predict the UCS of HSC composites, such as non-linear regression and linear regression. However, it is still challenging to conduct accurate prediction by applying simple regression models and advanced techniques are in great demand [35,36].

To overcome the above difficulties, machine learning (ML) algorithms have been developed rapidly for predicting the USC of concrete materials. ML models make predictions and decisions by building a mathematical model without being explicit programming based on sample data [37–39]. Many ML models have been used to predict concrete strength, such as neural networks, support vector regression (SVR), and tree-based models [40–43]. For instance, Huynh et al., (2020) [44] utilised artificial neural network (ANN), deep neural network (DNN), and deep residual network (ResNet) to predict the compressive strength of fly ash-based geopolymer concrete. Besides, the deep neural network (DNN) has been applied to perform structural reliability analysis and structural damage detection of truss structures [45,46]. The Extreme Learning Machine (ELM) and ANN were applied and compared to predict the compressive strength of concrete containing fly ash and silica fume [47]. The estimations of moment and rotation in steel rack connections and beam-to-column connections were implemented through ELM [48,49]. Mohammadhassani et al., (2014) [50] used an Adaptive Neuro-Fuzzy Inference System (ANFIS) to predict the shear strength of high strength concrete (HSC) beams without stirrups. The ML models can also be used to further propose multi-objective optimisation design [51–53]. Among most ML models, the back-propagation neural network (BPNN) demonstrates superior predicting capacity for solving engineering problems. The main reason is that BPNN is fast and easy to program without parameters to tune apart from the number of neurons in the hidden layer [54–56]. Therefore, BPNN is chosen as the prediction ML model in this study.

Generally, the number of hidden layers and the optimal number of neurons in each hidden layer are two parameters which significantly affect the performance of BPNN. To determine the two values, traditional trial and error methods are widely used, which is a waste of effort and time. To overcome the shortcoming, some meta-heuristic algorithms were developed for ML model optimisation. Genetic Algorithm (GA) and Particle Swarm Optimization (PSO) accompanied with ANN were applied for properties prediction [57,58]. These meta-heuristic algorithms also have extensive use in other ML models. For instance, Sharafati et al., (2020) [59,60] developed a combination of adaptive neuro-fuzzy inference system (ANFIS) with several meta-heuristic algorithms (e.g., PSO) to predict the shear strength of HSC slender beam and compressive strength of foamed concrete. A SVR-GA was employed to predict the shear strength of reinforced concrete (RC) deep beams [61]. Multivariate Adaptive Regression Splines optimized using Water Cycle Algorithm (MARS-WCA) was developed for the prediction of the compressive strength of concrete [62]. The grey wolf optimizer (GWO) was implemented with ELM to predict the compressive strength of concrete with partial replacements for cement [63]. It also successfully predicts the behaviour of channel shear connectors in composite floor systems at different temperatures [64]. A Support Vector Machine (SVM) coupled with Firefly Algorithm (FFA) was performed for the shear capacity estimation of angle shear connectors [65]. The Beetle Antennae Search (BAS) is another feasible meta-heuristic algorithm to tune BPNN architecture with fast convergence, stability in local optimization and uncomplicated implementation [41,66,67]. Therefore, BAS algorithm is chosen to tune the hyperparameters of BPNN. Some robust optimisers are also proposed recently such as adaptive hybrid evolutionary firefly algorithm (AHEFA), hybrid differential evolution and symbiotic organisms search (HDS), and evolutionary symbiotic organisms search algorithm (ESOS) [68–70].

In this study, the focus is on predicting the UCS of HSC using BAS-BPNN and understanding the sensitivity ranking of varying influencing factors upon the strength performance of HSC. Different from the traditional ML models, this study develops a novel ML model comprising BPNN and BAS architectures based on a total of 324 experiment data from the literature. The BAS algorithm possesses fast convergence which is beneficial to analysis on the basis of a large database. This pioneering research supplies a novel method to predict the mechanical strength of HSC for advanced engineering construction and application.

2. Dataset

A total of 324 HSC data samples are collected from previous literature [71] (listed in the Appendix A). Type 1 ordinary Portland cement (OPC) is used as binder material. Silica sand is incorporated as fine aggregate (FA) and the gravel with the size less than 20 mm is served as coarse gravel aggregate (CA). A polycarboxylate-based superplasticizer (SP) with a density of 1.06 g/cm^3 is also introduced for adjusting the cement fluidity and segregation performance.

The specific statistics of the input and output variables are summarised in Table 1 based on the database (Appendix A). All the five influencing variables comprise the content of cement, fine and coarse aggregates, water, and SP. The correlation coefficient distribution is computed, as shown demonstrated in Figure 1. According to the result, the UCS is highly correlated with cement. For input variables, most of the correlations are relatively low (less than 0.5), suggesting that these variables will not produce multicollinearity problems [72–74].

Table 1. Chart of input and output statistics.

ID	Data	Unit	Minimum	Maximum	Mean Value
Cement	Input	kg/m^3	284	600	417
Water	Input	kg/m^3	160	180	170
Coarse Aggregate	Input	kg/m^3	845	989	899
Fine Aggregate	Input	kg/m^3	552	951	768
SP	Input	kg/m^3	0	2	0.95
UCS	Output	MPa	37.5	73.6	52

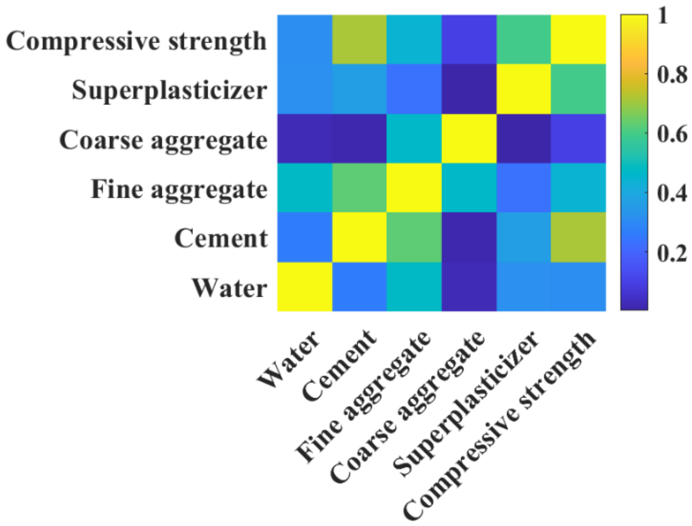

Figure 1. Correlation matrix of the variables of HSC.

3. Methodology

3.1. BPNN

The artificial neural network (ANN) is one of the commonly used machine learning models, which comprises many categories such as recurrent neural networks (RNN) and feedforward neural network (FFNN). The FFNN includes the Back-propagation neural network (BPNN), which is widely employed to solve problems in the field of building materials and construction [42,75,76]. Back propagation (BP) is a popular approach to adjust the weights and bias of the model, which is composed of an input layer, one or more hidden layers, and one output layer. The BP process will compare the actual outputs and predicted outputs to obtain the optimal weight and threshold values of the network. The output (O) of a neuron is computed as follow

$$O = f\left(\sum_{j=1}^{n}(w_j x_j) + b\right), \text{ UCS (MPa)} \quad (1)$$

where w_j represents the weight value of the jth input neuron (x_j) in the previous layer; b is the bias value of the output neuron; f denotes the activation function. In this study, the following active function was used mainly due to its superior performance [75]:

$$f(x) = \frac{2}{1 + \exp(-x)} - 1 \quad (2)$$

In the backpropagation process, the method computes the gradient of the error function with respect to the weights of the neural networks. The training iteration will stop when the mean square error (MSE) between the actual and predicted outputs become smaller than a defined threshold. The topology of the backpropagation process is shown in Figure 2.

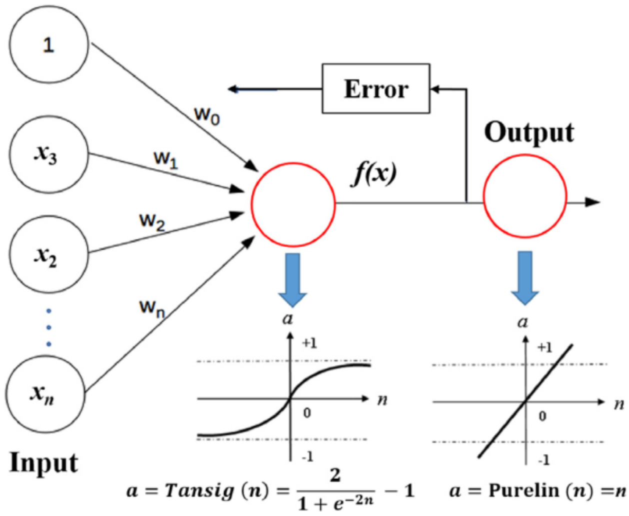

Figure 2. Backpropagation in the BPNN.

3.2. BAS

The BAS algorithm is a recently proposed metaheuristic optimization algorithm [77]. It is inspired by the hunting behavior of the longhorn beetle with its two long antennae. The beetle gradually moves to the food source (the global optimum). Therefore, the concentration of odour is represented by the objective function at position $\mathbf{x}$. In a multi-dimensional space, the global optimum (source point) lies in the position with the best objective value. The beetle's searching behaviour is given by:

$$\mathbf{x}_r = \mathbf{x}^i + d^i\mathbf{b} \tag{3}$$

$$\mathbf{x}_l = \mathbf{x}^i - d^i\mathbf{b} \tag{4}$$

where $\mathbf{x}_r$ and $\mathbf{x}_l$ represent the areas in the right-hand side and left-hand side, respectively; $\mathbf{x}^i$ is the position at an ith time instant. d^i denotes the length of the beetle's antennae at ith iteration. $\mathbf{b}$ denotes a unit vector that is randomly normalized, which is expressed as

$$\mathrm{b} = \frac{\mathrm{rnd}(\mathrm{k}, 1)}{\|\mathrm{rnd}(\mathrm{k}, 1)\|} \tag{5}$$

where k denotes the dimensionality of the position; $\mathrm{rnd}(\cdot)$ is a random function.

The beetle's detecting behaviour is determined using the following equation:

$$\mathbf{x}^{i+1} = \mathbf{x}^i + \delta^i\mathbf{b}\cdot\mathrm{sign}(f(\mathbf{x}_r) - f(\mathbf{x}_l)) \tag{6}$$

where $\mathrm{sign}(\cdot)$ is the sign function; δ^i represents the step size at the ith iteration, which is updated using the following formula:

$$\delta^{i+1} = \eta\delta^i \tag{7}$$

where η is the attenuation coefficient of the step size.

The flowchart of BAS is shown in Figure 3 and the pseudocode of tuning hyperparameters of BPNN using BAS is presented in Figure 4.

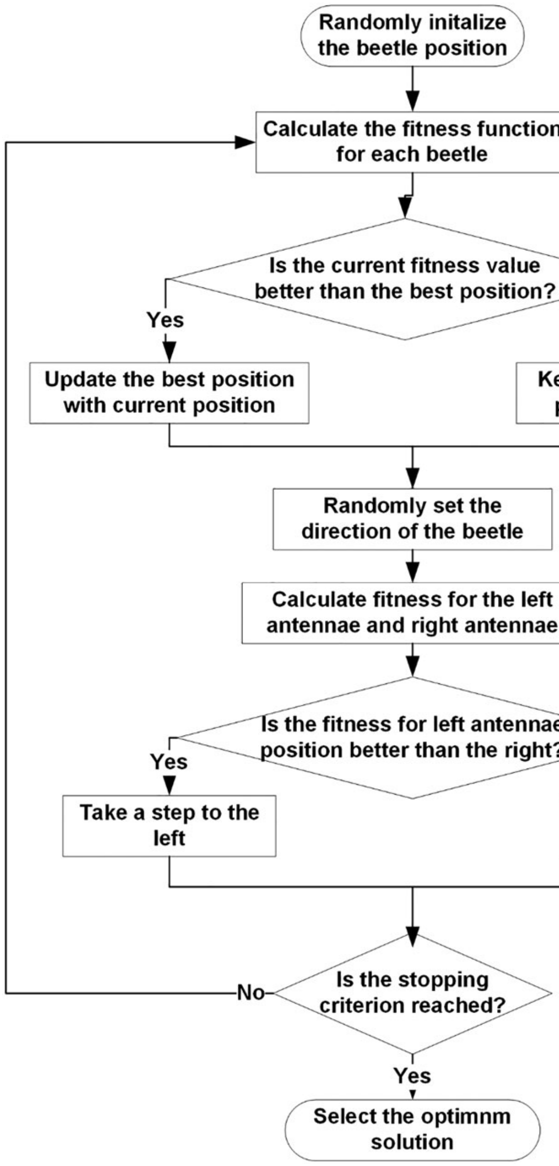

Figure 3. Flowchart of BAS.

Input: Training set $\boldsymbol{D_t}$ and validation set $\boldsymbol{D_v}$ from dataset $\boldsymbol{D}$, BPNN training and testing process BPNN ($\boldsymbol{D}$, $\boldsymbol{x^i}$), initial hyperparameter set $\boldsymbol{x^0}$
Output: Optimised hyperparameters $\boldsymbol{x_b}$, maximum iteration $\boldsymbol{n}$
For $i = 1$ to n
Calculate the left and right positions $\boldsymbol{x_l}$ and $\boldsymbol{x_r}$ of the beetle
Calculate the Root-mean-square error (RMSE) values in $\boldsymbol{D_v}$ for implementing BPNN ($\boldsymbol{D}$, $\boldsymbol{x_l}$) and BPNN ($\boldsymbol{D}$, $\boldsymbol{x_r}$) with hyperparameters $\boldsymbol{x_l}$ and $\boldsymbol{x_r}$, respectively
Calculate the next position $\boldsymbol{x^{i+1}}$
Calculate the RMSE in $\boldsymbol{D_v}$ in process BPNN ($\boldsymbol{D}$, $\boldsymbol{x^{i+1}}$) with hyperparameter $\boldsymbol{x^{i+1}}$
Update $\boldsymbol{x_b}$
$i = i + 1$
End

Figure 4. The pseudocode of tuning hyperparameters of BPNN using BAS, reprinted from ref. [78].

3.3. Performance Evaluation

In this study, Root-mean-square error (RMSE) and Correlation coefficient (R) are used to evaluate the performance of the proposed model. RMSE and R are calculated as follows

$$\text{RMSE} = \sqrt{\frac{1}{n}\sum_{i=1}^{n}\left(y_i^* - y_i\right)^2},\ \text{MPa} \tag{8}$$

where n denotes the number of data samples; y_i^* is the predicted value; y_i represents the actual value;

$$R = \frac{\sum_{i=1}^{n}\left(y_i^* - \overline{y^*}\right)\left(y_i - \overline{y}\right)}{\sqrt{\sum_{i=1}^{n}\left(y_i^* - \overline{y^*}\right)^2}\sqrt{\sum_{i=1}^{n}\left(y_i - \overline{y}\right)^2}},\ \text{dimensionless} \tag{9}$$

where and are the mean value of predicted and observed values, respectively.

3.4. Determination of Architecture of BPNN

The hidden layer and the number of neurons in each hidden layer are optimised using BAS in this study. To tune these hyperparameters, 10-fold cross validation (CV) was performed in the training set (Figure 5). The training set is divided into 10 folds, in which 9 folds are used to tune the number of neurons by BAS, and the performance of the BPNN model with the optimal architecture is validated in the remaining fold. After repeating 10 times (for each time, a different fold is selected as the validation fold), the average neuron number is selected as the final neuron number used in this study. Finally, 30% of the data in the test set are used to test the performance of the BPNN with optimal architecture.

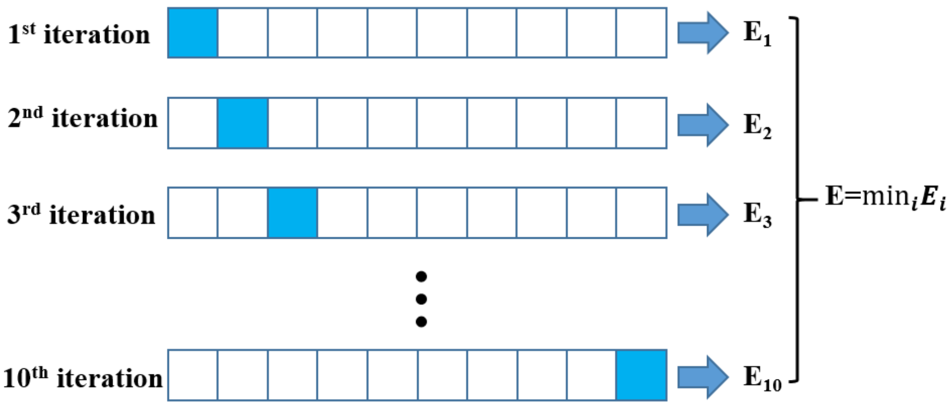

Figure 5. 10-fold cross validation.

4. Results and Discussion

4.1. Results of Hyperparameter Tuning

In this study, the number of neurons in each layer is tuned using the BAS algorithm. In each fold, the RMSE obtained by the BPNN (with optimal neuron number of this fold) is plotted in Figure 6. The smallest RMSE values versus iterations corresponding to varying hidden layers are shown in Figure 7, which presents the process of neuron number tuning. It can be seen that the RMSE decreases to its minimum value within 40 iterations, suggesting that BAS has high efficiency in finding the optimal number of neurons. Ultimately, the final hidden layer is 1 and the corresponding optimal neuron number is 24.

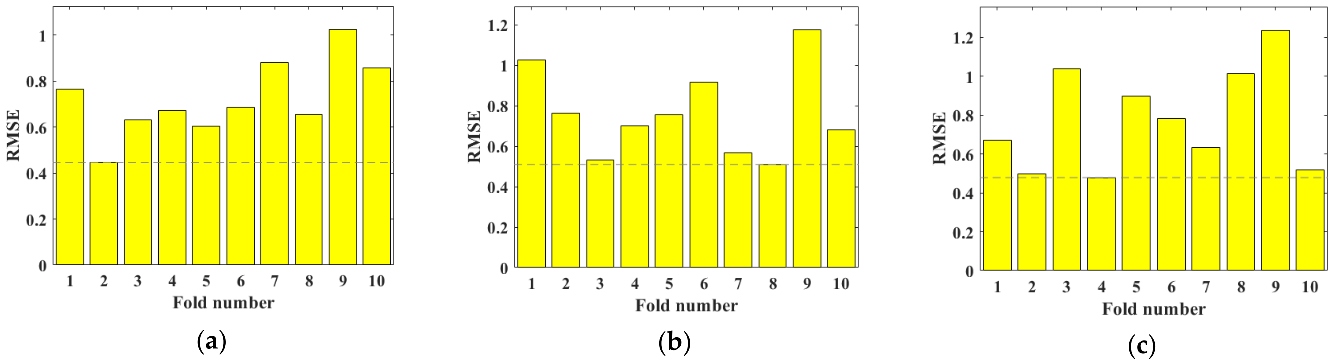

Figure 6. RMSE value in each fold when hidden layer is 1 (**a**), 2 (**b**), and 3 (**c**).

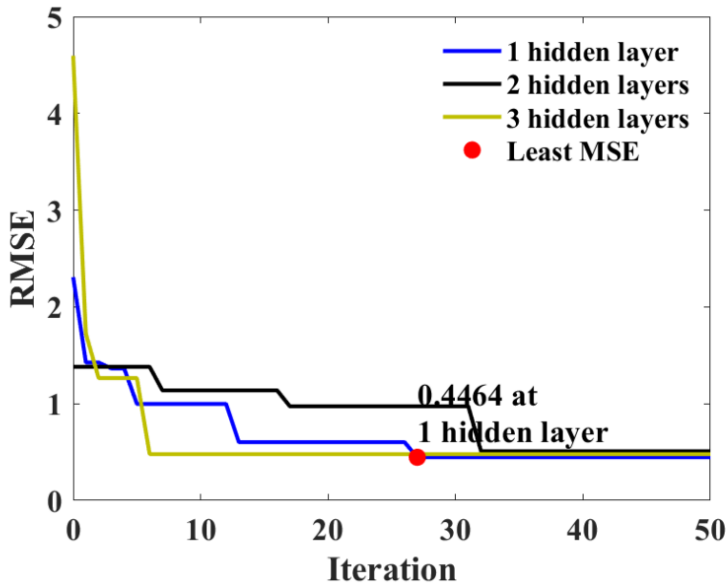

Figure 7. The lowest RMSE versus iteration corresponding to different hidden layers.

4.2. Performance of the BAS-BPNN Model

Figure 8 shows the actual values (blue line), predicted values (red point), and errors between the actual and predicted UCS (yellow bar graph). It can be observed that although several large noises are observed, most of the errors are pretty small on the training set (Figure 8a) and test set (Figure 8b). This result indicates that the BAS-BPNN model is highly accurate. The correlation between the actual and predicted UCS is visualized in Figure 9. High prediction accuracy is observed on the training set (Figure 9a) and test set (Figure 9b), as indicated by the high R values (0.9971 and 0.9893 on the training and test sets, respectively) and low RMSE values (0.7167 MPa and 1.5158 MPa on the training and test sets, respectively). Compared with previously published papers [42,51], the obtained results show much higher accuracy (R is around 0.99), which might be attributed to the model performance or the accuracy and size of the database. Furthermore, no overfitting problems take place as the test set RMSE (and R) is close to that on the training set. Owing to the inherent stochastic properties of the BAS algorithm, the statistical outcomes of extra 20 run times are also reported in Table 2 to verify the robustness of the introduced ML model.

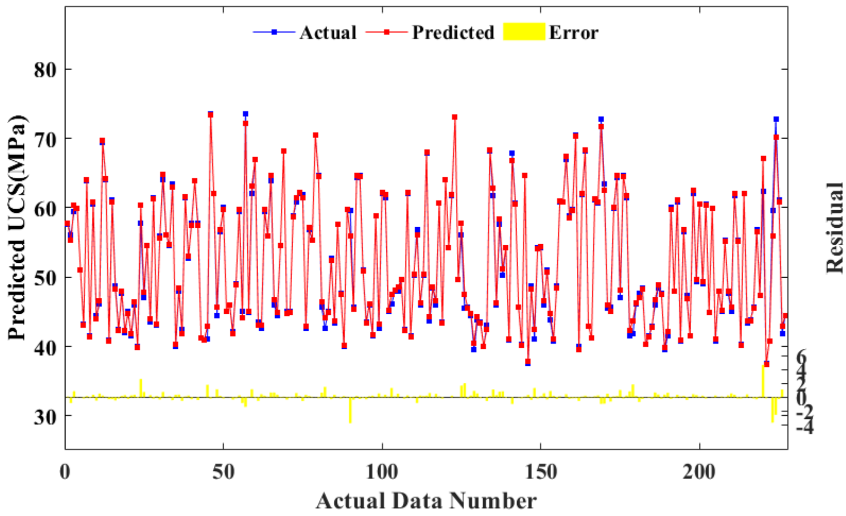

(**a**)

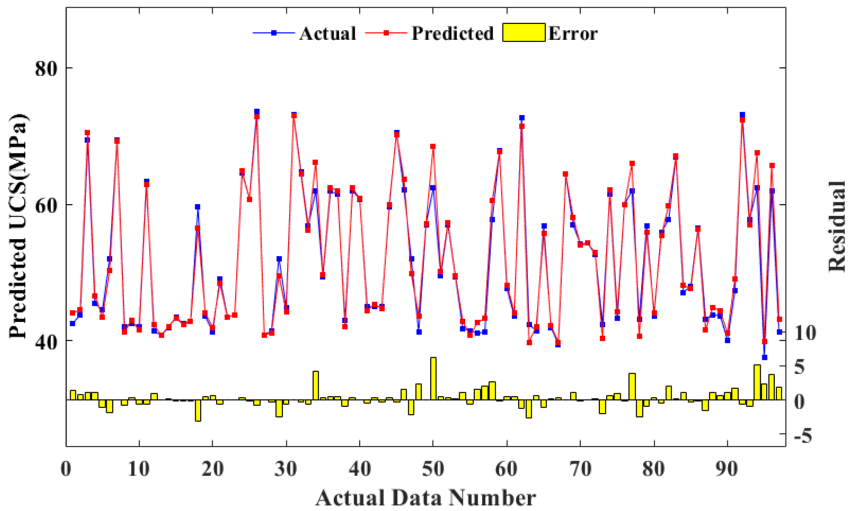

(**b**)

Figure 8. The error between actual and predicted UCS values on the training set (**a**) and test set (**b**).

Table 2. Statistical outcomes (RMSE, R) of the BAS-BPNN for the extra 20 run times.

Run Time	RMSE of Training and Test Sets (MPa)	R of Training and Test Sets	Run Time	RMSE of Training and Test Sets (MPa)	R of Training and Test Sets
1	1.0036, 1.1543	0.9945, 0.9922	11	1.3392, 1.1305	0.9893, 0.9942
2	1.0879, 1.3876	0.9933, 0.9894	12	0.9725, 1.0086	0.9949, 0.9937
3	0.8851, 1.2874	0.9956, 0.9906	13	1.1523, 1.1125	0.9929, 0.9919
4	1.0482, 1.0455	0.9935, 0.9945	14	1.1654, 1.3617	0.9925, 0.9898
5	1.3044, 1.6762	0.9914, 0.9844	15	0.9353, 1.0637	0.9951, 0.9940
6	0.8887, 1.1730	0.9955, 0.9927	16	1.1210, 1.3923	0.9929, 0.9891
7	1.0657, 1.2421	0.9940, 0.9919	17	1.1539, 1.3263	0.9928, 0.9896
8	0.9304, 1.8270	0.9953, 0.9804	18	1.2006, 1.2839	0.9925, 0.9901
9	0.9678, 1.3371	0.9948, 0.9898	19	0.9878, 1.2744	0.9945, 0.9913
10	1.2053, 1.5601	0.9921, 0.9875	20	0.8121, 1.1521	0.9960, 0.9945

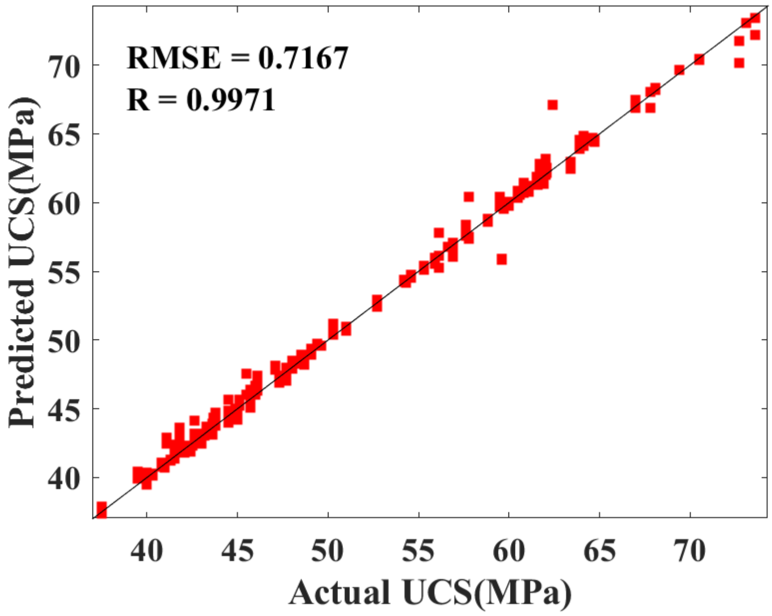

(**a**)

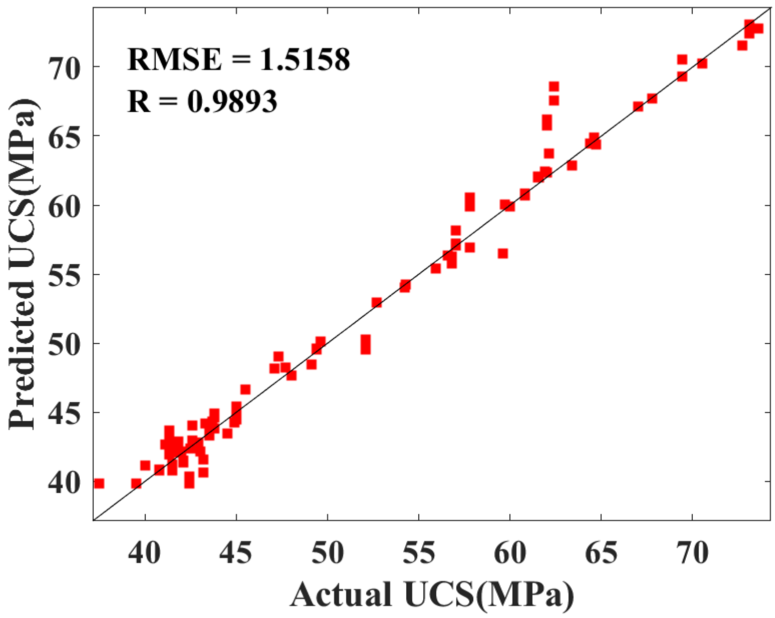

(**b**)

Figure 9. Predicted UCS versus actual UCS on the training set (**a**) and test set (**b**).

4.3. Variable Importance

Global sensitivity analysis (GSA) is combined with the developed BPNN model to analyse the variable importance (Figure 10). It can measure the impact on the proposed BAS-BPNN output when the input value changes within its value range [79]. The data sample is represented as x, and x_a, $a \in \{1, \ldots, M\}$ denotes an input variable through its range with L levels (M is the number of input variables). And y represents the UCS value which is predicted by the BPNN. According to the range of x_a and L levels, the input variable x_a can be divided into i values, namely, x_{ai}, $i = \{1, \ldots, L\}$. The respective sensitivity response of each input variable is calculated by Equation (10). Afterward, the relative importance of each variable is calculated by Equation (11).

$$g_a = \sum_{i=2}^{L} \frac{|\hat{y_{a,i}} - \hat{y_{a,i-1}}|}{L-1} \tag{10}$$

$$R_a = g_a / \sum_{i=1}^{L} g_i \tag{11}$$

where a is the input variable that needs to be analysed; $\hat{y_{a,i}}$, $i = \{1, \ldots, L\}$ stands for the sensitivity response indicator for x_{ai}, $i = \{1, \ldots, L\}$; R_a is the relative importance of the variable.

It can be observed that UCS of HSC is the most sensitive to contents of cement and water with importance ratios of 44.9% and 34.9%, respectively. This is mainly due to the water-to-cement ratio, which is crucial to the development of concrete strength. It is interesting to note that superplasticiser (importance ratio = 2.7%) is not as important as other influencing variables. This may be caused by insufficient content of superplasticiser in the concrete mixtures. It is worthwhile to note that the importance of input variables is calculated on the basis of the data set collected in this study, as listed in the Appendix A.

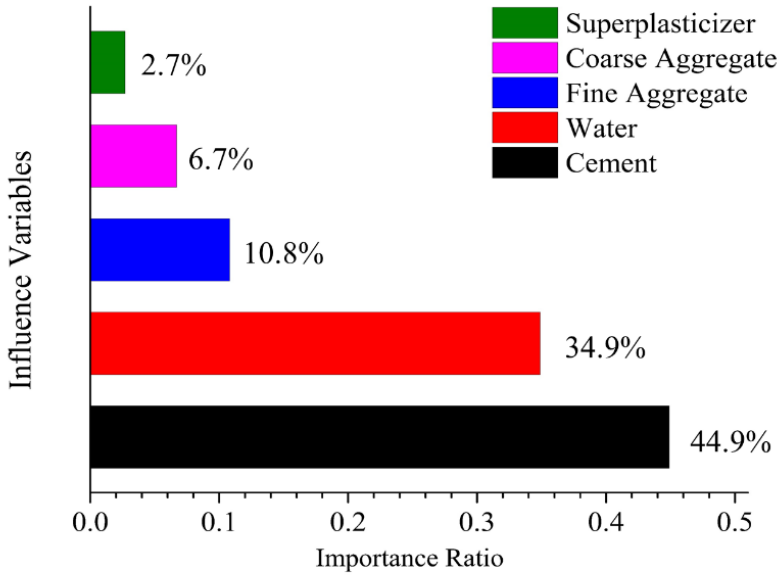

Figure 10. Variable importance of the input variables.

4.4. Comparison of the BAS-BPNN Model with Other ML Models

To seek the optimal ML model and further verify the strength of the established BAS-BPNN model in the prediction of UCS of HSC, its prediction performance is compared with several widely used ML models [80]: Support vector machine (SVM), random forest (RF), K-nearest neighbours (KNN), logistic regression (LR), and multiple-linear regression (MLR). Among these models, the hyperparameters of SVM, RF, and KNN are also tuned by BAS. The tuned hyperparameters with their empirical scopes, initial values, and final values are listed in Table 3. The hyperparameter tuning process of these models is shown in Figure 11. It can be seen that all RMSE curves can converge within 50 iterations, indicating the high searching efficiency of the BAS algorithm. In the first 20 iterations, the RMSE obtained by SVM decreases less significantly in comparison with that obtained by other ML models. This implies the initial hyperparameters of SVM are close to the optimal hyperparameters.

Table 3. Hyperparameters of different models.

Classifier	Hyperparameter	Empirical Scope	Initial Value	Final Value
SVM	Coefficient of the penalty term	[1,1000]	16	18.73
	Gamma value of gaussian kernel	[0.1,10]	16	34.88
RF	The minimum number of samples required to split an internal node	[1,10]	40	1
	The total number of trees	[2,100]	40	83
KNN	Number of neighbor samples	[1,10]	30	2

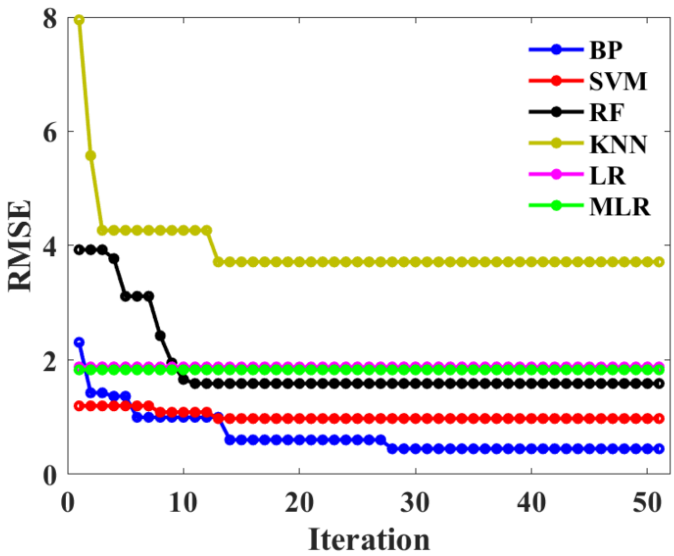

Figure 11. Hyperparameter tuning by different models on the training set.

The prediction errors of different ML models are compared on the test set using a boxplot, as shown in Figure 12. The lower edge of the box represents the first quartile, and the upper edge is the third quartile. The median is demonstrated as a red line in the box. The lower and upper whiskers are the 1.5 IQR minus the first quartile and 1.5 IQR above the third quartile, respectively (IQR is the interquartile range). All the other data points are defined as outliers in this study. It can be observed that BPNN has the smallest third quartile, indicating that most of the errors obtained by BPNN are relatively small. Although few outliers were observed in BPNN, the general prediction performance was the best among these ML models. The advantage of BAS-BPNN is also verified by comparing different ML models using a Taylor plot that shows in Figure 13, indicating three model evaluation indices (standard deviation, RMSE, and R). The ML model will be the most realistic if the distance between the ML model and the point labelled "Actual" is the shortest. It can be seen that BPNN is the closest to the "Actual point", suggesting BPNN performs better in terms of standard deviation, correlation coefficient, and RMSE. Generally, the boxplot and Taylor plot present a similar phenomenon, ranking the accuracy of ML models as BP, SVM, RF, MLR, LR, and KNN. This is controlled according to the model complexity and database suitability. According to the "no free lunch" (NFL) theorem of machine learning, there is no single model that performs universally superior to other models for any dataset. Therefore, based on the dataset used in this study, BPNN is the optimal prediction model.

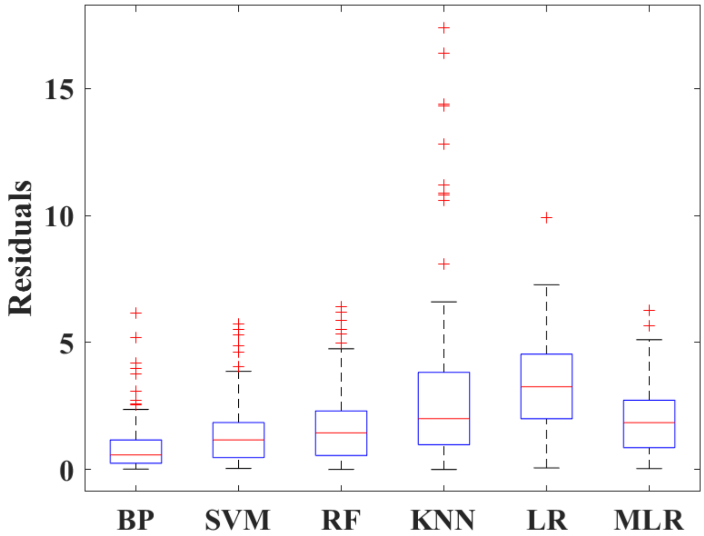

Figure 12. Boxplot showing the errors between predicted and actual UCS values on the test sets for different models.

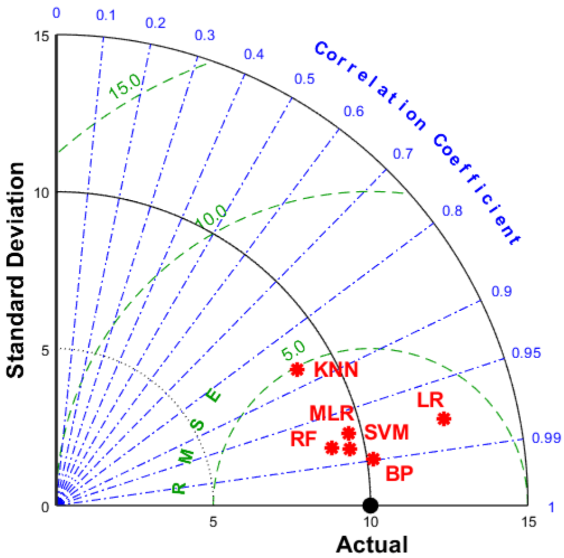

Figure 13. Taylor plot showing the errors between predicted and actual UCS values on the test sets for different models.

5. Conclusions

In this study, the BPNN model with the BAS algorithm being used to tune the hyperparameters was established to predict the UCS of HSC. The proposed BAS-BPNN model was developed based on a collected dataset containing over 300 HSC samples with different mixtures. The BPNNs with 1, 2, and 3 hidden layers were compared and the ultimate optimal architecture is one hidden layer with 24 neurons. The results show that BAS has high efficiency in tuning hyperparameters of BPNN and the obtained BAS-BPNN model is highly accurate (R = 0.9893, RMSE = 1.5158 MPa on the test set). Besides, the BAS-BPNN is superior by comparing its prediction performance with other widely used ML models (SVM, RF, KNN, LR, and MLR). In addition, the importance ranking of the input variables through GSA was implemented showing that cement and water are the most significant variables to the UCS of HSC. Generally, the findings in this study can be used in practice to support the HSC mix design.

It is noted that only five input variables are considered in this study, which inevitably influences the diversity and size of the database. Therefore, more samples containing varying raw materials such as fly ash, slags, and other solid wastes will be incorporated in the future to further improve the generalisation ability of the BAS-BPNN model. Also, other active functions, advanced machine learning models, and optimization algorithms (e.g., AHEFA, HDS, and ESOS) can be applied for performance comparison. An Adaptive Neuro-Fuzzy Inference System can be used to determine the most influencing parameters to further verify the findings in this study [81,82].

Author Contributions: Conceptualization, J.S.; methodology, J.S.; software, Y.W.; validation, Z.Z.; formal analysis, J.W.; investigation, R.H.; resources, C.P.; data curation, C.Z.; writing—original draft preparation, J.H.; writing—review and editing, Y.W.; visualization, Y.W.; supervision, X.W.; project administration, J.S.; funding acquisition, X.W. All authors have read and agreed to the published version of the manuscript.

Funding: This research is funded by the Academic Research Council of Australia Linkage Projects for Asset Intelligence: Maximising Operational Effectiveness for Digital Era, (Grant No. LP180100222); It is also supported by State Key Laboratory for GeoMechanics and Deep Underground Engineering, China University of Mining & Technology/China University of Mining & Technology, Beijing) (SKLGDUEK2105).

Data Availability Statement: The data presented in this study are openly available.

Conflicts of Interest: The authors declare no conflict of interest.

Appendix A

ID	Water (kg/m^3)	OPC (kg/m^3)	FA (kg/m^3)	CA (kg/m^3)	SP (kg/m^3)	UCS (MPa)
1	160	533	805	845	1	73.6
2	160	533	805	845	1.5	73.6
3	160	533	805	845	2	73.6
4	160	480	786	845	1	73.1
5	160	480	786	845	1.5	73.1
6	160	480	786	845	2	73.1
7	160	427	767	845	1	72.7
8	160	427	767	845	1.5	72.7
9	160	427	767	845	2	72.7
10	160	533	753	898	1	69.4
11	160	533	753	898	1.5	69.4
12	160	533	753	898	2	69.4
13	160	480	734	898	1	70.5
14	160	480	734	898	1.5	70.5
15	160	480	734	898	2	70.5
16	160	427	715	898	1	68.1
17	160	427	715	898	1.5	68.1
18	160	427	715	898	2	68.1
19	160	533	701	950	1	67.8
20	160	533	701	950	1.5	67.8
21	160	533	701	950	2	67.8
22	160	480	682	950	1	67
23	160	480	682	950	1.5	67
24	160	480	682	950	2	67
25	160	427	663	950	1	64.1
26	160	427	663	950	1.5	64.1
27	160	427	663	950	2	64.1
28	170	567	751	845	1	64.6
29	170	567	751	845	1.5	64.6
30	170	567	751	845	2	64.6
31	170	510	731	845	1	64.4

ID	Water (kg/m^3)	OPC (kg/m^3)	FA (kg/m^3)	CA (kg/m^3)	SP (kg/m^3)	UCS (MPa)
32	170	510	731	845	1.5	64.4
33	170	510	731	845	2	64.4
34	170	453	711	845	1	64.7
35	170	453	711	845	1.5	64.7
36	170	453	711	845	2	64.7
37	170	567	700	898	1	63.9
38	170	567	700	898	1.5	63.9
39	170	567	700	898	2	63.9
40	170	510	679	898	1	63.4
41	170	510	679	898	1.5	63.4
42	170	510	679	898	2	63.4
43	170	453	659	898	1	62
44	170	453	659	898	1.5	62
45	170	453	659	898	2	62
46	170	567	648	950	1	62.4
47	170	567	648	950	1.5	62.4
48	170	567	648	950	2	62.4
49	170	510	628	950	1	61.7
50	170	510	628	950	1.5	61.7
51	170	510	628	950	2	61.7
52	170	453	608	950	1	61.9
53	170	453	608	950	1.5	61.9
54	170	453	608	950	2	61.9
55	180	600	698	845	0.75	59.5
56	180	600	698	845	1.25	59.5
57	180	600	698	845	1.75	59.5
58	180	540	677	845	0.75	61.1
59	180	540	677	845	1.25	61.1
60	180	540	677	845	1.75	61.1
61	180	480	655	845	0.75	60.8
62	180	480	655	845	1.25	60.8
63	180	480	655	845	1.75	60.8
64	180	600	646	898	0.75	60.5
65	180	600	646	898	1.25	60.5
66	180	600	646	898	1.75	60.5
67	180	540	625	898	0.75	59.9
68	180	540	625	898	1.25	59.9
69	180	540	625	898	1.75	59.9
70	180	480	604	898	0.75	57
71	180	480	604	898	1.25	57
72	180	480	604	898	1.75	57
73	180	600	594	950	0.75	59.7
74	180	600	594	950	1.25	59.7
75	180	600	594	950	1.75	59.7
76	180	540	573	950	0.75	60
77	180	540	573	950	1.25	60
78	180	540	573	950	1.75	60
79	180	480	552	950	0.75	59.6
80	180	480	552	950	1.25	59.6
81	180	480	552	950	1.75	59.6
82	160	457	867	845	0.75	62
83	160	457	867	845	1.25	62
84	160	457	867	845	1.75	62
85	160	411	851	845	0.75	62
86	160	411	851	845	1.25	62
87	160	411	851	845	1.75	62

ID	Water (kg/m^3)	OPC (kg/m^3)	FA (kg/m^3)	CA (kg/m^3)	SP (kg/m^3)	UCS (MPa)
88	160	366	835	845	0.75	60.6
89	160	366	835	845	1.25	60.6
90	160	366	835	845	1.75	60.6
91	160	457	816	898	0.75	62.1
92	160	457	816	898	1.25	62.1
93	160	457	816	898	1.75	62.1
94	160	411	799	898	0.75	61.5
95	160	411	799	898	1.25	61.5
96	160	411	799	898	1.75	61.5
97	160	366	783	898	0.75	57.8
98	160	366	783	898	1.25	57.8
99	160	366	783	898	1.75	57.8
100	160	457	764	950	0.75	61.5
101	160	457	764	950	1.25	61.5
102	160	457	764	950	1.75	61.5
103	160	411	747	950	0.75	60.8
104	160	411	747	950	1.25	60.8
105	160	411	747	950	1.75	60.8
106	160	366	731	950	0.75	57.6
107	160	366	731	950	1.25	57.6
108	160	366	731	950	1.75	57.6
109	170	486	818	845	0.5	58.8
110	170	486	818	845	1	58.8
111	170	486	818	845	1.5	58.8
112	170	437	801	845	0.5	56.8
113	170	437	801	845	1	56.8
114	170	437	801	845	1.5	56.8
115	170	389	783	845	0.5	55.3
116	170	389	783	845	1	55.3
117	170	389	783	845	1.5	55.3
118	170	486	766	898	0.5	57.8
119	170	486	766	898	1	57.8
120	170	486	766	898	1.5	57.8
121	170	437	749	898	0.5	56.6
122	170	437	749	898	1	56.6
123	170	437	749	898	1.5	56.6
124	170	389	732	898	0.5	56.9
125	170	389	732	898	1	56.9
126	170	389	732	898	1.5	56.9
127	170	486	714	950	0.5	56.1
128	170	486	714	950	1	56.1
129	170	486	714	950	1.5	56.1
130	170	437	697	950	0.5	55.9
131	170	437	697	950	1	55.9
132	170	437	697	950	1.5	55.9
133	170	389	680	950	0.5	54.3
134	170	389	680	950	1	54.3
135	170	389	680	950	1.5	54.3
136	180	514	769	845	0.25	54.2
137	180	514	769	845	0.75	54.2
138	180	514	769	845	1.25	54.2
139	180	463	750	845	0.25	52.7
140	180	463	750	845	0.75	52.7
141	180	463	750	845	1.25	52.7
142	180	411	732	845	0.25	51
143	180	411	732	845	0.75	51
144	180	411	732	845	1.25	51
145	180	514	717	898	0.25	54.6
146	180	514	717	898	0.75	54.6

ID	Water (kg/m^3)	OPC (kg/m^3)	FA (kg/m^3)	CA (kg/m^3)	SP (kg/m^3)	UCS (MPa)
147	180	514	717	898	1.25	54.6
148	180	463	698	898	0.25	50.3
149	180	463	698	898	0.75	50.3
150	180	463	698	898	1.25	50.3
151	180	411	680	898	0.25	47.3
152	180	411	680	898	0.75	47.3
153	180	411	680	898	1.25	47.3
154	180	514	665	950	0.25	52.1
155	180	514	665	950	0.75	52.1
156	180	514	665	950	1.25	52.1
157	180	463	647	950	0.5	45.5
158	180	463	647	950	1	45.5
159	180	463	647	950	1.5	45.5
160	180	411	628	950	0.5	45.7
161	180	411	628	950	1	45.7
162	180	411	628	950	1.5	45.7
163	160	400	914	845	0.5	49.6
164	160	400	914	845	1	49.6
165	160	400	914	845	1.5	49.6
166	160	360	900	845	0.5	48
167	160	360	900	845	1	48
168	160	360	900	845	1.5	48
169	160	320	886	845	0.5	47.7
170	160	320	886	845	1	47.7
171	160	320	886	845	1.5	47.7
172	160	400	863	989	0.5	49.1
173	160	400	863	989	1	49.1
174	160	400	863	989	1.5	49.1
175	160	360	848	898	0.5	48
176	160	360	848	898	1	48
177	160	360	848	898	1.5	48
178	160	320	834	898	0.5	48.5
179	160	320	834	898	1	48.5
180	160	320	834	898	1.5	48.5
181	160	400	811	950	0.5	49.4
182	160	400	811	950	1	49.4
183	160	400	811	950	1.5	49.4
184	160	360	797	950	0.5	48.7
185	160	360	797	950	1	48.7
186	160	360	797	950	1.5	48.7
187	160	320	782	950	0.5	46.1
188	160	320	782	950	1	46.1
189	160	320	782	950	1.5	46.1
190	170	425	868	845	0	47.7
191	170	425	868	845	0.5	47.7
192	170	425	868	845	1	47.7
193	170	425	853	845	0	47.1
194	170	425	853	845	0.5	47.1
195	170	425	853	845	1	47.1
196	170	340	838	845	0	45
197	170	340	838	845	0.5	45
198	170	340	838	845	1	45
199	170	425	816	898	0	46
200	170	425	816	898	0.5	46
201	170	425	816	898	1	46
202	170	383	801	898	0	45.7
203	170	383	801	898	0.5	45.7
204	170	383	801	898	1	45.7
205	170	340	786	898	0	45.1

ID	Water (kg/m^3)	OPC (kg/m^3)	FA (kg/m^3)	CA (kg/m^3)	SP (kg/m^3)	UCS (MPa)
206	170	340	786	898	0.5	45.1
207	170	340	786	898	1	45.1
208	170	425	764	950	0	46
209	170	425	764	950	0.5	46
210	170	425	764	950	1	46
211	170	383	749	950	0	45
212	170	383	749	950	0.5	45
213	170	383	749	950	1	45
214	170	340	734	950	0	43.3
215	170	340	734	950	0.5	43.3
216	170	340	734	950	1	43.3
217	180	450	821	845	0	44.5
218	180	450	821	845	0.5	44.5
219	180	450	821	845	1	44.5
220	180	405	805	845	0	43.6
221	180	405	805	845	0.5	43.6
222	180	405	805	845	1	43.6
223	180	360	789	845	0	42
224	180	360	789	845	0.5	42
225	180	360	789	845	1	42
226	180	450	770	898	0	43.8
227	180	450	770	898	0.5	43.8
228	180	450	770	898	1	43.8
229	180	405	754	898	0	43
230	180	405	754	898	0.5	43
231	180	405	754	898	1	43
232	180	360	738	898	0	43.2
233	180	360	738	898	0.5	43.2
234	180	360	738	898	1	43.2
235	180	450	718	950	0	43.5
236	180	450	718	950	0.5	43.5
237	180	450	718	950	1	43.5
238	180	405	702	950	0	41.5
239	180	405	702	950	0.5	41.5
240	180	405	702	950	1	41.5
241	180	360	686	950	0	42.4
242	180	360	686	950	0.5	42.4
243	180	360	686	950	1	42.4
244	160	356	951	845	0.5	46
245	160	356	951	845	1	46
246	160	356	951	845	1.5	46
247	160	320	938	845	0.5	45
248	160	320	938	845	1	45
249	160	320	938	845	1.5	45
250	160	284	926	845	0.5	43.7
251	160	284	926	845	1	43.7
252	160	284	926	845	1.5	43.7
253	160	356	899	898	0.5	44.5
254	160	356	899	898	1	44.5
255	160	356	899	898	1.5	44.5
256	160	320	886	898	0.5	42.6
257	160	320	886	898	1	42.6
258	160	320	886	898	1.5	42.6
259	160	284	874	898	0.5	43.8
260	160	284	874	898	1	43.8
261	160	284	874	898	1.5	43.8
262	160	356	847	950	0.5	43.6
263	160	356	847	950	1	43.6

ID	Water (kg/m^3)	OPC (kg/m^3)	FA (kg/m^3)	CA (kg/m^3)	SP (kg/m^3)	UCS (MPa)
264	160	356	847	950	1.5	43.6
265	160	320	835	950	0.5	42.6
266	160	320	835	950	1	42.6
267	160	320	835	950	1.5	42.6
268	160	284	822	950	0.5	42.9
269	160	284	822	950	1	42.9
270	160	284	822	950	1.5	42.9
271	170	378	907	845	0.5	44.9
272	170	378	907	845	1	44.9
273	170	378	907	845	1.5	44.9
274	170	340	893	845	0	41.1
275	170	340	893	845	0.5	41.1
276	170	340	893	845	1	41.1
277	170	302	880	845	0	41.5
278	170	302	880	845	0.5	41.5
279	170	302	880	845	1	41.5
280	170	378	855	898	0	42.5
281	170	378	855	898	0.5	42.5
282	170	378	855	898	1	42.5
283	170	340	842	898	0	40.8
284	170	340	842	898	0.5	40.8
285	170	340	842	898	1	40.8
286	170	302	828	898	0	40.8
287	170	302	828	898	0.5	40.8
288	170	302	828	898	1	40.8
289	170	378	803	950	0	41.8
290	170	378	803	950	0.5	41.8
291	170	378	803	950	1	41.8
292	170	340	790	950	0	41.3
293	170	340	790	950	0.5	41.3
294	170	340	790	950	1	41.3
295	170	302	776	950	0	41
296	170	302	776	950	0.5	41
297	170	302	776	950	1	41
298	180	400	863	845	0	41.3
299	180	400	863	845	0.5	41.3
300	180	400	863	845	1	41.3
301	180	360	848	845	0	41.5
302	180	360	848	845	0.5	41.5
303	180	360	848	845	1	41.5
304	180	320	834	845	0	40.3
305	180	320	834	845	0.5	40.3
306	180	320	834	845	1	40.3
307	180	400	811	898	0	41.5
308	180	400	811	898	0.5	41.5
309	180	400	811	898	1	41.5
310	180	360	797	898	0	40
311	180	360	797	898	0.5	40
312	180	360	797	898	1	40
313	180	320	782	898	0	40
314	180	320	782	898	0.5	40
315	180	320	782	898	1	40
316	180	400	759	950	0	42.1
317	180	400	759	950	0.5	42.1
318	180	400	759	950	1	42.1

ID	Water (kg/m^3)	OPC (kg/m^3)	FA (kg/m^3)	CA (kg/m^3)	SP (kg/m^3)	UCS (MPa)
319	180	360	745	950	0	39.5
320	180	360	745	950	0.5	39.5
321	180	360	745	950	1	39.5
322	180	320	731	950	0	37.5
323	180	320	731	950	0.5	37.5
324	180	320	731	950	1	37.5

References

1. Carrasquillo, R.L.; Nilson, A.H.; Slate, F.O. Properties of High Strength Concrete Subjectto Short-Term Loads. *J. Proc.* **1981**, *78*, 171–178.
2. Zhang, W.; Tang, Z.; Yang, Y.; Wei, J.; Stanislav, P. Mixed-Mode Debonding Behavior between CFRP Plates and Concrete under Fatigue Loading. *J. Struct. Eng.* **2021**, *147*, 04021055. [CrossRef]
3. Dehghani, A.; Hayatdavoodi, A.; Aslani, F. The ultimate shear capacity of longitudinally stiffened steel-concrete composite plate girders. *J. Constr. Steel Res.* **2021**, *179*, 106550. [CrossRef]
4. Mbessa, M.; Péra, J. Durability of high-strength concrete in ammonium sulfate solution. *Cem. Concr. Res.* **2001**, *31*, 1227–1231. [CrossRef]
5. Zhang, W.; Tang, Z. Numerical Modeling of Response of CFRP–Concrete Interfaces Subjected to Fatigue Loading. *J. Compos. Constr.* **2021**, *25*, 04021043. [CrossRef]
6. Hayatdavoodi, A.; Dehghani, A.; Aslani, F.; Nateghi-Alahi, F. The development of a novel analytical model to design composite steel plate shear walls under eccentric shear. *J. Build. Eng.* **2021**, *44*, 103281. [CrossRef]
7. Wang, Q.; Wang, D.; Chen, H. The role of fly ash microsphere in the microstructure and macroscopic properties of high-strength concrete. *Cem. Concr. Compos.* **2017**, *83*, 125–137. [CrossRef]
8. Xu, S.; Wang, J.; Shou, W.; Ngo, T.; Sadick, A.-M.; Wang, X. Computer vision techniques in construction: A critical review. *Arch. Comput. Methods Eng.* **2021**, *28*, 3383–3397. [CrossRef]
9. Dehghani, A.; Mozafari, A.R.; Aslani, F. Evaluation of the efficacy of using engineered cementitious composites in RC beam-column joints. *Structures* **2020**, *27*, 151–162. [CrossRef]
10. Saradar, A.; Tahmouresi, B.; Mohseni, E.; Shadmani, A. Restrained shrinkage cracking of fiber-reinforced high-strength concrete. *Fibers* **2018**, *6*, 12. [CrossRef]
11. Aslani, F.; Deghani, A.; Gunawardena, Y. Experimental investigation of the behavior of concrete-filled high-strength glass fiber-reinforced polymer tubes under static and cyclic axial compression. *Struct. Concr.* **2020**, *21*, 1497–1522. [CrossRef]
12. Dehghani, A.; Aslani, F. Fatigue performance and design of concrete-filled steel tubular joints: A critical review. *J. Constr. Steel Res.* **2019**, *162*, 105749. [CrossRef]
13. Shariati, M.; Sulong, N.R.; Kueh, A. Comparative performance of channel and angle shear connectors in high strength concrete composites: An experimental study. *Constr. Build. Mater.* **2016**, *120*, 382–392. [CrossRef]
14. Shariati, A.; Shariati, M.; Sulong, N.H.R.; Suhatril, M.; Khanouki, M.A.; Mahoutian, M. Experimental assessment of angle shear connectors under monotonic and fully reversed cyclic loading in high strength concrete. *Constr. Build. Mater.* **2014**, *52*, 276–283. [CrossRef]
15. Mohammadhassani, M.; Akib, S.; Shariati, M.; Suhatril, M.; Khanouki, M.A. An experimental study on the failure modes of high strength concrete beams with particular references to variation of the tensile reinforcement ratio. *Eng. Fail. Anal.* **2014**, *41*, 73–80. [CrossRef]
16. Sun, J.; Huang, Y.; Aslani, F.; Wang, X.; Ma, G. Mechanical enhancement for EMW-absorbing cementitious material using 3D concrete printing. *J. Build. Eng.* **2021**, *41*, 102763. [CrossRef]
17. Sun, J.; Aslani, F.; Wei, J.; Wang, X. Electromagnetic absorption of copper fiber oriented composite using 3D printing. *Constr. Build. Mater.* **2021**, *300*, 124026. [CrossRef]
18. Singh, V.; Gu, N.; Wang, X. A theoretical framework of a BIM-based multi-disciplinary collaboration platform. *Autom. Constr.* **2011**, *20*, 134–144. [CrossRef]
19. Sun, J.; Aslani, F.; Lu, J.; Wang, L.; Huang, Y.; Ma, G. Fresh and mechanical behaviour of developed fibre-reinforced lightweight engineered cementitious composites for 3D concrete printing containing hollow glass microspheres. *Ceram. Int.* **2021**, *47*, 27107–27121. [CrossRef]
20. Liu, J.; Wu, C.; Wu, G.; Wang, X. A novel differential search algorithm and applications for structure design. *Appl. Math. Comput.* **2015**, *268*, 246–269. [CrossRef]
21. Sun, J.; Huang, Y.; Aslani, F.; Ma, G. Properties of a double-layer EMW-absorbing structure containing a graded nano-sized absorbent combing extruded and sprayed 3D printing. *Constr. Build. Mater.* **2020**, *261*, 120031. [CrossRef]
22. Sun, J.; Huang, Y.; Aslani, F.; Ma, G. Electromagnetic wave absorbing performance of 3D printed wave-shape copper solid cementitious element. *Cem. Concr. Compos.* **2020**, *114*, 103789. [CrossRef]

23. Ma, G.; Sun, J.; Aslani, F.; Huang, Y.; Jiao, F. Review on electromagnetic wave absorbing capacity improvement of cementitious material. *Constr. Build. Mater.* **2020**, *262*, 120907. [CrossRef]
24. Sun, J.; Wang, Y.; Liu, S.; Dehghani, A.; Xiang, X.; Wei, J.; Wang, X. Mechanical, chemical and hydrothermal activation for waste glass reinforced cement. *Constr. Build. Mater.* **2021**, *301*, 124361. [CrossRef]
25. Li, J.; Qin, Q.; Sun, J.; Ma, Y.; Li, Q. Mechanical and conductive performance of electrically conductive cementitious composite using graphite, steel slag, and GGBS. *Struct. Concr.* **2020**. [CrossRef]
26. Aslani, F.; Dehghani, A.; Wang, L. The effect of hollow glass microspheres, carbon nanofibers and activated carbon powder on mechanical and dry shrinkage performance of ultra-lightweight engineered cementitious composites. *Constr. Build. Mater.* **2021**, *280*, 122415. [CrossRef]
27. Dehghani, A.; Aslani, F.; Panah, N.G. Effects of initial SiO_2/Al_2O_3 molar ratio and slag on fly ash-based ambient cured geopolymer properties. *Constr. Build. Mater.* **2021**, *293*, 123527. [CrossRef]
28. Aslani, F.; Deghani, A.; Asif, Z. Development of lightweight rubberized geopolymer concrete by using polystyrene and recycled crumb-rubber aggregates. *J. Mater. Civ. Eng.* **2020**, *32*, 04019345. [CrossRef]
29. Aslani, F.; Sun, J.; Huang, G. Mechanical behavior of fiber-reinforced self-compacting rubberized concrete exposed to elevated temperatures. *J. Mater. Civ. Eng.* **2019**, *31*, 04019302. [CrossRef]
30. Aslani, F.; Sun, J.; Bromley, D.; Ma, G. Fiber-reinforced lightweight self-compacting concrete incorporating scoria aggregates at elevated temperatures. *Struct. Concr.* **2019**, *20*, 1022–1035. [CrossRef]
31. Aslani, F.; Hou, L.; Nejadi, S.; Sun, J.; Abbasi, S. Experimental analysis of fiber-reinforced recycled aggregate self-compacting concrete using waste recycled concrete aggregates, polypropylene, and steel fibers. *Struct. Concr.* **2019**, *20*, 1670–1683. [CrossRef]
32. Sun, J.; Lin, S.; Zhang, G.; Sun, Y.; Zhang, J.; Chen, C.; Morsy, A.M.; Wang, X. The effect of graphite and slag on electrical and mechanical properties of electrically conductive cementitious composites. *Constr. Build. Mater.* **2021**, *281*, 122606. [CrossRef]
33. Feng, J.; Chen, B.; Sun, W.; Wang, Y. Microbial induced calcium carbonate precipitation study using Bacillus subtilis with application to self-healing concrete preparation and characterization. *Constr. Build. Mater.* **2021**, *280*, 122460. [CrossRef]
34. Aslani, F.; Gunawardena, Y.; Dehghani, A. Behaviour of concrete filled glass fibre-reinforced polymer tubes under static and flexural fatigue loading. *Constr. Build. Mater.* **2019**, *212*, 57–76. [CrossRef]
35. Sun, J.; Ma, Y.; Li, J.; Zhang, J.; Ren, Z.; Wang, X. Machine learning-aided design and prediction of cementitious composites containing graphite and slag powder. *J. Build. Eng.* **2021**, *43*, 102544. [CrossRef]
36. Sun, J.; Wang, Y.; Yao, X.; Ren, Z.; Zhang, G.; Zhang, C.; Chen, X.; Ma, W.; Wang, X. Machine-Learning-Aided Prediction of Flexural Strength and ASR Expansion for Waste Glass Cementitious Composite. *Appl. Sci.* **2021**, *11*, 6686. [CrossRef]
37. Zhang, J.; Sun, Y.; Li, G.; Wang, Y.; Sun, J.; Li, J. Machine-learning-assisted shear strength prediction of reinforced concrete beams with and without stirrups. *Eng. Comput.* **2020**, *36*, 1–15. [CrossRef]
38. Wu, C.; Wang, X.; Chen, M.; Kim, M.J. Differential received signal strength based RFID positioning for construction equipment tracking. *Adv. Eng. Inform.* **2019**, *42*, 100960. [CrossRef]
39. Wang, L.; Yuan, J.; Wu, C.; Wang, X. Practical algorithm for stochastic optimal control problem about microbial fermentation in batch culture. *Optim. Lett.* **2019**, *13*, 527–541. [CrossRef]
40. Sun, Y.; Zhang, J.; Li, G.; Wang, Y.; Sun, J.; Jiang, C. Optimized neural network using beetle antennae search for predicting the unconfined compressive strength of jet grouting coalcretes. *Int. J. Numer. Anal. Methods Geomech.* **2019**, *43*, 801–813. [CrossRef]
41. Sun, Y.; Zhang, J.; Li, G.; Ma, G.; Huang, Y.; Sun, J.; Nener, B. Determination of Young's modulus of jet grouted coalcretes using an intelligent model. *Eng. Geol.* **2019**, *252*, 43–53. [CrossRef]
42. Feng, W.; Wang, Y.; Sun, J.; Tang, Y.; Wu, D.; Jiang, Z.; Wang, J.; Wang, X. Prediction of thermo-mechanical properties of rubber-modified recycled aggregate concrete. *Constr. Build. Mater.* **2022**, *318*, 125970. [CrossRef]
43. Sun, Y.; Li, G.; Zhang, J.; Sun, J.; Huang, J.; Taherdangkoo, R. New Insights of Grouting in Coal Mass: From Small-Scale Experiments to Microstructures. *Sustainability* **2021**, *13*, 9315. [CrossRef]
44. Huynh, A.T.; Nguyen, Q.D.; Xuan, Q.L.; Magee, B.; Chung, T.; Tran, K.T.; Nguyen, K.T. A machine learning-assisted numerical predictor for compressive strength of geopolymer concrete based on experimental data and sensitivity analysis. *Appl. Sci.* **2020**, *10*, 7726. [CrossRef]
45. Lieu, Q.X.; Nguyen, K.T.; Dang, K.D.; Lee, S.; Kang, J.; Lee, J. An adaptive surrogate model to structural reliability analysis using deep neural network. *Expert Syst. Appl.* **2022**, *189*, 116104. [CrossRef]
46. Lee, S.; Park, S.; Kim, T.; Lieu, Q.X.; Lee, J. Damage quantification in truss structures by limited sensor-based surrogate model. *Appl. Acoust.* **2021**, *172*, 107547. [CrossRef]
47. Shariati, M.; Armaghani, D.J.; Khandelwal, M.; Zhou, J.; Khorami, M. Assessment of longstanding effects of fly ash and silica fume on the compressive strength of concrete using extreme learning machine and artificial neural network. *J. Adv. Eng. Comput.* **2021**, *5*, 50–74. [CrossRef]
48. Shariati, M.; Trung, N.T.; Wakil, K.; Mehrabi, P.; Safa, M.; Khorami, M. Estimation of moment and rotation of steel rack connections using extreme learning machine. *Steel Compos. Struct.* **2019**, *31*, 427–435.
49. Trung, N.T.; Shahgoli, A.F.; Zandi, Y.; Shariati, M.; Wakil, K.; Safa, M.; Khorami, M. Moment-rotation prediction of precast beam-to-column connections using extreme learning machine. *Struct. Eng. Mech.* **2019**, *70*, 639–647.

50. Mohammadhassani, M.; Nezamabadi-Pour, H.; Suhatril, M.; Shariati, M. An evolutionary fuzzy modelling approach and comparison of different methods for shear strength prediction of high-strength concrete beams without stirrups. *Smart Struct. Syst. Int. J.* **2014**, *14*, 785–809. [CrossRef]
51. Sun, J.; Wang, X.; Zhang, J.; Xiao, F.; Sun, Y.; Ren, Z.; Zhang, G.; Liu, S.; Wang, Y. Multi-objective optimisation of a graphite-slag conductive composite applying a BAS-SVR based model. *J. Build. Eng.* **2021**, *44*, 103223. [CrossRef]
52. Sun, Y.; Li, G.; Zhang, J.; Sun, J.; Xu, J. Development of an ensemble intelligent model for assessing the strength of cemented paste backfill. *Adv. Civ. Eng.* **2020**, *2020*, 1643529. [CrossRef]
53. Zhang, C.; Ali, A. The advancement of seismic isolation and energy dissipation mechanisms based on friction. *Soil Dyn. Earthq. Eng.* **2021**, *146*, 106746. [CrossRef]
54. Chandwani, V.; Agrawal, V.; Nagar, R. Modeling slump of ready mix concrete using genetic algorithms assisted training of Artificial Neural Networks. *Expert Syst. Appl.* **2015**, *42*, 885–893. [CrossRef]
55. Tang, Y.; Feng, W.; Chen, Z.; Nong, Y.; Guan, S.; Sun, J. Fracture behavior of a sustainable material: Recycled concrete with waste crumb rubber subjected to elevated temperatures. *J. Clean. Prod.* **2021**, *318*, 128553. [CrossRef]
56. Zhao, R.; Zhang, L.; Guo, B.; Chen, Y.; Fan, G.; Jin, Z.; Guan, X.; Zhu, J. Unveiling substitution preference of chromium ions in sulphoaluminate cement clinker phases. *Compos. Part B Eng.* **2021**, *222*, 109092. [CrossRef]
57. Shariati, M.; Mafipour, M.S.; Mehrabi, P.; Ahmadi, M.; Wakil, K.; Trung, N.T.; Toghroli, A. Prediction of concrete strength in presence of furnace slag and fly ash using Hybrid ANN-GA (Artificial Neural Network-Genetic Algorithm). *Smart Struct. Syst.* **2020**, *25*, 183–195.
58. Shariati, M.; Mafipour, M.S.; Mehrabi, P.; Bahadori, A.; Zandi, Y.; Salih, M.N.A.; Nguyen, H.; Dou, J.; Song, X.; Poi-Ngian, S. Application of a hybrid artificial neural network-particle swarm optimization (ANN-PSO) model in behavior prediction of channel shear connectors embedded in normal and high-strength concrete. *Appl. Sci.* **2019**, *9*, 5534. [CrossRef]
59. Sharafati, A.; Haghbin, M.; Aldlemy, M.S.; Mussa, M.H.; Al Zand, A.W.; Ali, M.; Bhagat, S.K.; Al-Ansari, N.; Yaseen, Z.M. Development of advanced computer aid model for shear strength of concrete slender beam prediction. *Appl. Sci.* **2020**, *10*, 3811. [CrossRef]
60. Sharafati, A.; Naderpour, H.; Salih, S.Q.; Onyari, E.; Yaseen, Z.M. Simulation of foamed concrete compressive strength prediction using adaptive neuro-fuzzy inference system optimized by nature-inspired algorithms. *Front. Struct. Civ. Eng.* **2021**, *15*, 61–79. [CrossRef]
61. Zhang, G.; Ali, Z.H.; Aldlemy, M.S.; Mussa, M.H.; Salih, S.Q.; Hameed, M.M.; Al-Khafaji, Z.S.; Yaseen, Z.M. Reinforced concrete deep beam shear strength capacity modelling using an integrative bio-inspired algorithm with an artificial intelligence model. *Eng. Comput.* **2020**, *36*, 1–14. [CrossRef]
62. Ashrafian, A.; Shokri, F.; Amiri, M.J.T.; Yaseen, Z.M.; Rezaie-Balf, M. Compressive strength of Foamed Cellular Lightweight Concrete simulation: New development of hybrid artificial intelligence model. *Constr. Build. Mater.* **2020**, *230*, 117048. [CrossRef]
63. Shariati, M.; Mafipour, M.S.; Ghahremani, B.; Azarhomayun, F.; Ahmadi, M.; Trung, N.T.; Shariati, A. A novel hybrid extreme learning machine–grey wolf optimizer (ELM-GWO) model to predict compressive strength of concrete with partial replacements for cement. *Eng. Comput.* **2020**, *36*, 1–23. [CrossRef]
64. Shariati, M.; Mafipour, M.S.; Mehrabi, P.; Zandi, Y.; Dehghani, D.; Bahadori, A.; Shariati, A.; Trung, N.T.; Poi-Ngian, S. Application of Extreme Learning Machine (ELM) and Genetic Programming (GP) to design steel-concrete composite floor systems at elevated temperatures. *Steel Compos. Struct.* **2019**, *33*, 319–332.
65. Chahnasir, E.S.; Zandi, Y.; Shariati, M.; Dehghani, E.; Toghroli, A.; Mohamad, E.T.; Shariati, A.; Safa, M.; Wakil, K.; Khorami, M. Application of support vector machine with firefly algorithm for investigation of the factors affecting the shear strength of angle shear connectors. *Smart Struct. Syst.* **2018**, *22*, 413–424.
66. Luo, Y.; Zheng, H.; Zhang, H.; Liu, Y. Fatigue reliability evaluation of aging prestressed concrete bridge accounting for stochastic traffic loading and resistance degradation. *Adv. Struct. Eng.* **2021**, *24*, 3021–3029. [CrossRef]
67. Mou, B.; Bai, Y. Experimental investigation on shear behavior of steel beam-to-CFST column connections with irregular panel zone. *Eng. Struct.* **2018**, *168*, 487–504. [CrossRef]
68. Lieu, Q.X.; Do, D.T.; Lee, J. An adaptive hybrid evolutionary firefly algorithm for shape and size optimization of truss structures with frequency constraints. *Comput. Struct.* **2018**, *195*, 99–112. [CrossRef]
69. Nguyen-Van, S.; Nguyen, K.T.; Luong, V.H.; Lee, S.; Lieu, Q.X. A novel hybrid differential evolution and symbiotic organisms search algorithm for size and shape optimization of truss structures under multiple frequency constraints. *Expert Syst. Appl.* **2021**, *184*, 115534. [CrossRef]
70. Nguyen-Van, S.; Nguyen, K.T.; Dang, K.D.; Nguyen, N.T.; Lee, S.; Lieu, Q.X. An evolutionary symbiotic organisms search for multiconstraint truss optimization under free vibration and transient behavior. *Adv. Eng. Softw.* **2021**, *160*, 103045. [CrossRef]
71. Al-Shamiri, A.K.; Kim, J.H.; Yuan, T.-F.; Yoon, Y.S. Modeling the compressive strength of high-strength concrete: An extreme learning approach. *Constr. Build. Mater.* **2019**, *208*, 204–219. [CrossRef]
72. Farrar, D.E.; Glauber, R.R. Multicollinearity in regression analysis: The problem revisited. *Rev. Econ. Stat.* **1967**, *49*, 92–107. [CrossRef]
73. Lu, N.; Wang, H.; Wang, K.; Liu, Y. Maximum Probabilistic and Dynamic Traffic Load Effects on Short-to-Medium Span Bridges. *Comput. Model. Eng. Sci.* **2021**, *127*, 345–360. [CrossRef]

74. Xu, J.; Lan, W.; Ren, C.; Zhou, X.; Wang, S.; Yuan, J. Modeling of coupled transfer of water, heat and solute in saline loess considering sodium sulfate crystallization. *Cold Reg. Sci. Technol.* **2021**, *189*, 103335. [CrossRef]
75. Zhang, J.; Huang, Y.; Wang, Y.; Ma, G. Multi-objective optimization of concrete mixture proportions using machine learning and metaheuristic algorithms. *Constr. Build. Mater.* **2020**, *253*, 119208. [CrossRef]
76. Ni, T.; Liu, D.; Xu, Q.; Huang, Z.; Liang, H.; Yan, A. Architecture of cobweb-based redundant TSV for clustered faults. *IEEE Trans. Very Large Scale Integr. (VLSI) Syst.* **2020**, *28*, 1736–1739. [CrossRef]
77. Wang, J.; Chen, H. BSAS: Beetle swarm antennae search algorithm for optimization problems. *arXiv* **2018**, arXiv:1807.10470.
78. Zhang, J.; Huang, Y.; Ma, G.; Nener, B. Mixture optimization for environmental, economical and mechanical objectives in silica fume concrete: A novel frame-work based on machine learning and a new meta-heuristic algorithm. *Resour. Conserv. Recycl.* **2021**, *167*, 105395. [CrossRef]
79. Cortez, P.; Embrechts, M.J. Using sensitivity analysis and visualization techniques to open black box data mining models. *Inf. Sci.* **2013**, *225*, 1–17. [CrossRef]
80. Zhang, J.; Wang, Y. Evaluating the bond strength of FRP-to-concrete composite joints using metaheuristic-optimized least-squares support vector regression. *Neural Comput. Appl.* **2021**, *33*, 3621–3635. [CrossRef]
81. Shariati, M.; Mafipour, M.S.; Haido, J.H.; Yousif, S.T.; Toghroli, A.; Trung, N.T.; Shariati, A. Identification of the most influencing parameters on the properties of corroded concrete beams using an Adaptive Neuro-Fuzzy Inference System (ANFIS). *Steel Compos. Struct.* **2020**, *34*, 155.
82. Safa, M.; Shariati, M.; Ibrahim, Z.; Toghroli, A.; Baharom, S.B.; Nor, N.M.; Petkovic, D. Potential of adaptive neuro fuzzy inference system for evaluating the factors affecting steel-concrete composite beam's shear strength. *Steel Compos. Struct.* **2016**, *21*, 679–688. [CrossRef]